Anal. Bioanal. Electrochem., Vol. 16, No. 11, 2024, 1026-1045
https://www.doi.org/10.22034/abec.2024.718628

Analytical & Bioanalytical Electrochemistry

2024 by CEE
www.abechem.com

Full Paper

Synthesis, Structural, Magnetic, And Electrochemical Properties of Er-Ni Doped Strontium Nanoferrites

A. Thippeswamy,[1] M.N. Manjunatha,[2] Prabhakar Chavan,[3] and G. Krishnamurthy[4,*]

[1]*Department of PG Studies in Industrial Chemistry, Government Arts and Science College (Autonomous), Karwar -581301, Karnataka, India*
[2]*Department of Chemistry, M.S. Ramaiah Institute of Technology, Bangalore, Karnataka, India*
[3]*Department of PG Studies and Research in Chemistry, Sahyadri Science College, Constituent College of Kuvempu University, Shivamogga, Karnataka, India -577203*
[4]*Department of PG Studies and Research in Chemistry and Industrial Chemistry, Sahyadri Science College, Constituent College of Kuvempu University, Shivamogga, Karnataka, India -577203*

*Corresponding Author, Tel.: +919448774649
E-Mail: gkmnaiksahyadri@gmail.com

Received: 22 August 2024 / Received in revised form: 27 November 2024 / Accepted: 28 November 2024 / Published online: 30 November 2024

Abstract- In the present study, erbium-doped nickel ferrites, $Ni_{0.5}Sr_{0.5}Er_xFe_{2-x}O_4$ ($x=0.00<x<0.09$) spinel nanoparticles were synthesized by the self-propagation method. Er^{3+} ions successfully doped into the spinel lattice of $Ni_{0.5}Sr_{0.5}Er_xFe_{2-x}O_4$ without any distortion. The influence of Er^{3+} ions on the structure, surface morphology, and magnetic behaviour has been determined by powder XRD, EF-SEM, DSC-TGA, VSM, etc., and PXRD confirmed the spinel nanocrystalline structure. SEM analysis showed the size is between 27-30 nm with irregular morphology and grain boundaries. EDAX confirms elements in the expected percentage. The weight loss due to the degradation of synthesised nanoparticles (NPs) was studied by TGA-DSC. VSM at room temperature confirms the cubic spinel structure and soft magnetic in nature and can be altered with a variation of Er^{3+} ions. The glassy carbon electrode (GCE) was modified by coating a layer of synthesized $Ni_{0.5}Sr_{0.5}Er_xFe_{2-x}O_4$ to detect the electron transfer reactions using cyclic voltammetry and also to sense the presence of Hg^{2+} in the polluted sample.

Keywords- Spinel lattice; Saturation magnetisation; Self propagation; Powder XRD; Cyclic voltammetry, Optical band gap

1. INTRODUCTION

Ferrites nanocomposites play an important role in revolutionised nano-world. Ferrite nanomaterials have been attracted because of their chemical, structural, optical, magnetic, and electrical properties. Doping of transition or inner transition metals into ferrites can improve specific properties of nanomaterials [1]. Doping leads to changes in physicochemical properties, and surface properties and has improved biocompatibility for remedial applications like magnetic nanofluids, specific drug delivery, magnetic resonance imaging (MRI), cell detachment, tissue fixing, biosensors etc. [2-7]. Doped nanoferrites also found to have photocatalytic, sensors, water decontamination, and ceramics properties. A literature survey reveals that nickel, a d^8 divalent metal cation which on doping in ferrites causes inverse spinel structure and such nanocomposites show ferromagnetic or superparmagnetic behaviour. $NiFe_2O_4$ has a particle size in the range 1-100 nm exhibits a high surface to volume ratio. In addition, erbium doped nickel nanoferrites undergo excellent structural modifications by occupying tetrahedral and octahedral sites. In a unit cell containing 32 oxygen atoms in a cubic close pack arrangement, half of the ferric ions fill the tetrahedral A-sites and represent the formula, ABO_4 (where A= Fe^{3+}, B = $Ni^{2+}$and Er^{3+}) [8,9]. The structure modifications are very critical in designing spinels depending upon their specific requirements. Generally, nickel ferrites are used as soft ferrites due to their low electrical conductivity and high electrochemical stability. Nickel combined with materials of relatively low electrical properties display low eddy current loss in alternating current applications [10]. It was also reported that the rare earth metal ion substitution leads to structural distortion but can have improvement in the electrical and magnetic properties. Rare earth ions have unpaired 4f electrons and undergo strong spin orbit coupling of angular momentum. Therefore, magnetic anisotropy is an important parameter that controls the magnetic transition temperature between superparamagnetic and ferromagnetic phases in rare-earth metal doped nanoparticles [11-14]. Some researchers have reported doping of certain rare-earth elements like Er^{3+}, La^{3+}, Ce^{3+}, Sm^{3+}, Dy^{3+} etc., to nano ferrites in order to improve their electrical, magnetic, and other properties. In this direction, erbium (Er^{3+}) doped nickel ferrites are of interest which can have soft ferrite materials with low Hc and high Ms value [15,16]. These concepts attracted more researchers over the last few decades.

Mercury is a heavy liquid metal on earth at room temperature and a toxic element, it is used in industrial instruments like batteries, thermometers, barometers, and switches. Mercury is a very hazardous element and causes very harmful effects on marine life and human organs. It irritates eyes, skin and causes stomach pain, chest pain, and headache. The deposition of mercury in animal systems affects neurological and behavioural disorders. Therefore, methods to detect Hg^{2+} are very essential. Literature showed that the cyclic voltammogram is a potential, sensitive, rapid and reliable method for the detection of Hg^{2+}. In our laboratory, the synthesis of NPs and the electrochemical detection of bioactive molecules using modified electrodes

have been done for the past few years [17-23]. In continuation of our research work, we report here the synthesis, characterization of $Ni_{0.5}Sr_{0.5}Er_xFe_{2-X}O_4$ NPs, their magnetic, electrochemical oxidation and detection of mercury (Hg^{2+}) in various concentrations.

2. EXPERIMENTAL SECTION

2.1. Materials

The nanoparticles (NPs) $Ni_{0.5}Sr_{0.5}Er_xFe_{2-x}O_4$ ($x=0.00<x<0.09$) were prepared via self-propagation (combustion method). The chemicals $Ni(NO_3)_2.6H_2O$ were purchased from Sigma Aldrich, $Sr(NO_3)_2$ from Himedia, $Fe(NO_3)_3.9H_2O$ from Sigma Aldrich, $Er(NO_3)_3.6H_2O$ and urea from Merck. In this method, the small quantity of Er^{3+} ion was substituted stoichiometrically and all chemicals were used without purification.

2.2 Synthesis of Erbium-doped nanoferrites

The calculated quantity of the respective metal salts was dissolved in deionised water in different beakers and mixed with urea as fuel and solutions were stirred to become homogeneous solutions. The stoichiometric ratio of each salt solution was taken in a petri-dish and then placed into a furnace at 550 ± 10 °C. Initially, the solution begins to boil in a furnace and then ignites finally releasing a mixture of gases (N_2O and CO_2). Due to the release of a certain amount of heat in the reaction, the homogeneous solution gets evaporated. The solution begins to burn when the solution reaches its self-ignition point and gives solidified mass which then becomes loose powder. This method of preparation gives better particle size and also reduces the diffusion distance related to unreacted particles closing together. All prepared $Ni_{0.5}Sr_{0.5}Er_xFe_{2-x}O_4$ NPs characterized by PXRD, FT-IR, FE-SEM, EDAX, TGA-DSC, Vibrating sample magnetometer (VSM), and Electrochemical analysis.

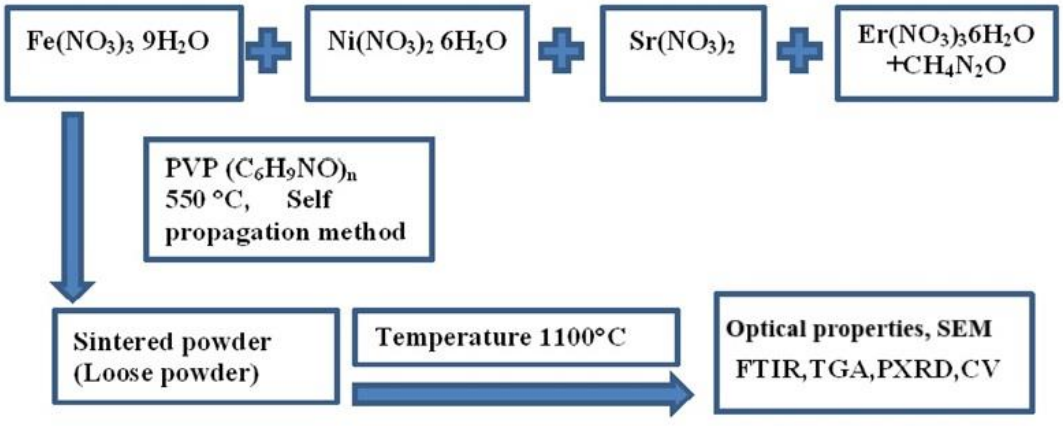

Scheme 1. Graphical representation of synthesis $Ni_{0.5}Sr_{0.5}Er_xFe_{2-x}O_4$ ($x=0.00<x<0.09$) nanoparticles

3. RESULTS AND DISCUSSION

3.1. Powder X-ray diffraction analysis

The synthesied $Ni_{0.5}Sr_{0.5}Er_xFe_{2-x}O_4$ (x=0.00<x<0.09) nanoferrites were determined using Bruker XRD with CuKα radiation having wavelength 1.5406 Å (Model: D8 Advance, Germany), in the Bragg angle range of 20 - 80° at a scan rate of 2° min at 300 K. The Figure 1 represents the diffraction patterns of different NPs. The peaks obtained in different spectral patterns were matched with the standard card, JCPDS card No. 86-2267 [24]. The lattice planes indexed as (110), (111), (220), (222), (311), (331), (400), (511), (440), (442) planes indicating the cubic spinel structure of nickel ferrite.

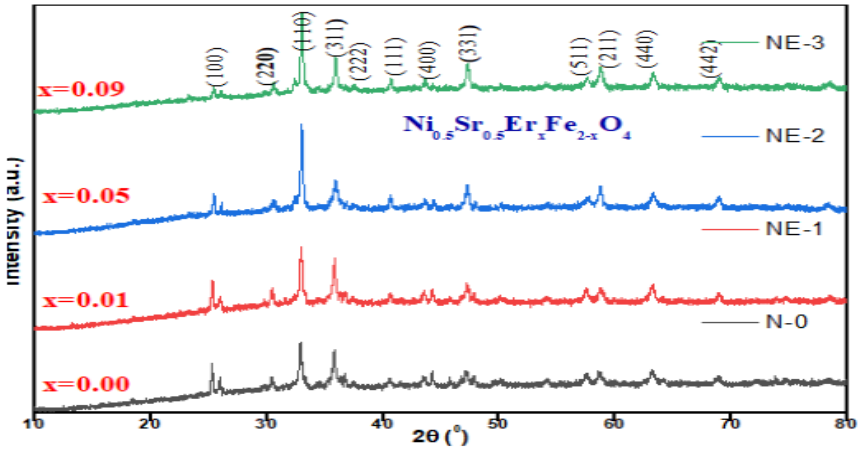

Figure 1. PXRD of $Ni_{0.5}Sr_{0.5}Er_xFe_{2-x}O_4$ (x=0.00<x<0.09) nanoferrites

The PXRD is used to evaluate structural parameters by using relations given below and the values are collected in Table 1.

$$a = d\sqrt{h^2 + k^2 + l^2} \quad Å \qquad (1)$$

where, a = lattice parameter utilizing these, the Bragg's angle (2θ) and interplanar spacing (d) were estimated[25, 26]. The Vcell is the unit of the cubic spinel ferrites and is determined by,

$$V\ cell = a^3 Å \qquad (2)$$

Using Debye-Scherrer equation (d), the numerical value is assisted for the spinel system. From the XRD peaks, the average crystallite sizes of the nanoferrites are determined and are calculated:

$$d = \frac{K\lambda}{\beta\cos\theta} \qquad (3)$$

where, K = 0.89 is Scherer's constant, λ = 0.15406 nm is wavelength of the incident X-rays in nm, β is the full width at half maximum (FWHM) of diffraction peak, θ is the Bragg's diffraction angle. The obtained values show that the average value of crystallite size is in the

range of 27-30 nm, which increases with Er^{3+} content. The lattice plane and different parameters are tabulated in Table 1. The measured X-ray density is calculated by using the relation as follows,

$$\rho x = \frac{8M}{Na3} \quad (4)$$

where M is the molecular weight of the sample, N the Avogadro's number, and a^3 the volume of the cubic unit cell. The bulk density is calculated by using the relation as mentioned below: where m is the mass, r is the radius and h is the height of the pellet. Percentage porosity was calculated using the formula:

$$\rho b = \frac{m}{\pi r^2 h} \quad (5)$$

where m is the mass, r is the radius and h is the height of the pellet. Percentage porosity was calculated using the formula:

$$P = \left(1 - \frac{\rho b}{\rho x}\right) \quad (6)$$

where, is the x-ray density and the bulk density.

Table 1. The crystallite size (D), lattice constant (a), cell volume (V), X-ray density (qx ray), bulk density, and percentage porosity of $Ni_{0.5}Sr_{0.5}Er_xFe_{2-x}O_4$ ($x=0.00<x<0.09$)

Composition	Crystallite size (D) /nm	Lattice constant (a)/Å	Cell volume (V)	X-ray density (qx -ray)/g cm^3	Bulk Density g/cm^3	Percentage Porosity (%)
$Ni_{0.5}Sr_{0.5}Fe_2O_4$	28.30	8.32	580.0	5.92	4.66	29.34
$Ni_{0.5}Sr_{0.5}Er_{0.01}Fe_{1.99}O_4$	27.94	8.44	603.3	8.18	6.75	19.17
$Ni_{0.5}Sr_{0.5}Er_{0.05}Fe_{1.95}O_{19}$	29.47	8.50	618.6	8.41	6.80	16.20
$Ni_{0.5}Sr_{0.5}Er_{0.09}Fe_{1.91}O_{19}$	30.48	8.54	633.4	7.90	6.82	13.30

The lattice constant (a) increases slightly for all the compositions and the variation can be explained on the basis of ionic radii of the substituted ions. The replacement of the smaller Fe^{3+} ions (0.64 Å) with larger Er^{3+} ions (0.93 Å) causes dilation of the host spinel lattice which results in the increase of lattice constant 8.32 to 8.54 Å without altering the crystal structure. The influence of erbium concentration on X-ray density (ρx) and bulk density(ρb) are tabulated in table 1. X-ray density increases from 5.92 to 8.41 g/cm^3 an increasing trend with erbium contents as it mainly depends upon the molecular weight of the samples. The bulk density also increases with erbium contents from 4.66 to 6.82 g/cm^3 which can be attributed to the difference in atomic weight of erbium (167.25 amu) and iron (55.845 amu) as described in CRC book [27]. The formation of the secondary phase ($Ni_{0.5}Sr_{0.5}Er_xFe_{2-x}O_4$) fills inter granular voids and exhibits good densification. Therefore, a decrease in the percentage porosity can be expected with Er^{3+} content which is collected in Table 1 [28].

3.2. FTIR analysis

The formation of functional groups was confirmed by Fourier transform infrared (FTIR) spectroscopy. At room temperature FTIR spectra of all nickel ferrites were recorded by employing Thermo-Nicolet 6700 FTIR (Make: Perkin Elmer, Model: Spectrum Two, USA) in the wavenumber range 4000 - 300 cm^{-1}. The samples (0.5 to 1.0 mg) were mixed with spectral grade potassium bromide (KBr) as the standard ground and then pressed to obtain circular discs of appropriate 1mm thickness. The FT-IR spectra of the prepared series of $Ni_{0.5}Sr_{0.5}Er_xFe_{2-x}O_4$ ($x=0.00<x<0.09$) nanoparticles are depicted in the supplementary file Figure S1. Two metal-oxygen (M–O) vibration modes were revealed by FT-IR spectra within the range of 1500 to 350 cm^{-1} confirming the successful formation of spinel ferrites. The first band (υ_1) with the maximum frequency was observed in the range 370 $cm^{-1}$and the second band (υ_2) with minimum frequency in the range 490 cm^{-1}, which indicates metal–oxygen stretching at tetrahedral (A) site and octahedral (B) site respectively [29]. The peaks with a wavenumber of ~ 800 cm^{-1} are due to the vibration of the Fe-OH bond. The stretching band slightly changed in Er^{3+} substituted nanoparticles. Therefore, the erbium replaces the Fe^{2+} ions without changing the crystal structure of the composition. In addition, the absence of bands in the region 3200 - 3500 cm^{-1} indicates the non-existence of an OH group [30]. The secondary potential energy is obtained by force constant and identified by the radius of the site. The force constants for tetrahedral and octahedral sites are given by the relations.

$$K_T = 4\pi^2c^2\nu_1^2m \qquad (7)$$

$$K_0 = 4\pi^2c^2\nu_2^2m \qquad (8)$$

Where υ_1 and υ_2 are the vibrational frequencies in cm^{-1} at A- and B-sites respectively, m-decreased mass of Fe^{3+} and O^{2-} ions and c - speed of light 2.99×10^8 m/s,. It is observed from Table 2, that the value of force constant from 0.2829-0.3814 newton/m for tetrahedral sites (KT) is lower than that for the octahedral site (KO) (0.3731-0.5055 N/m). Furthermore, the values KT and KO are found to be increased with an increase in Er^{3+} ion substitution [31].

Table 2. Position of IR absorption bands and force constant of of $Ni_{0.5}Sr_{0.5}Er_xFe_{2-x}O_4$ ($x=0.00<x<0.09$)

Composition	Position of ν_1(cm^{-1})	Force constant Tetrahedral (KT) newton/m	Position of ν_2 (cm^{-1})	Force constant Octahedral (KO) newton/m
$Ni_{0.5}Sr_{0.5}Fe_2O_4$	370	0.2829	488	0.3731
$Ni_{0.5}Sr_{0.5}Er_{0.01}Fe_{1.99}O_4$	369	0.3653	490	0.4851
$Ni_{0.5}Sr_{0.5}Er_{0.05}Fe_{1.95}O_{19}$	371	0.3738	491	0.4947
$Ni_{0.5}Sr_{0.5}Sm_{0.09}Fe_{1.91}O_{19}$	372	0.3814	493	0.5055

3.3. Field Emission Scanning Electron Microscopy (FE-SEM) analysis

The microstructure of pure nano ferrites of $Ni_{0.5}Sr_{0.5}Er_xFe_{2-x}O_4$ ($x=0.00<x<0.09$) were examined by FESEM (Model: JEOL/EO JSM-639, Germany) as shown in Figure 2. It is clear from the micro-graphs that both pure and Er^{3+} substituted nanoparticles have almost irregular morphology and grain boundaries are not prominent. The agglomeration of the particles is more visible in the nanoparticles, it is due to the accumulation of some Er^{3+} ions at grain boundaries instead of replacing Fe^{+3} ions at octahedral sites of spinel lattice.

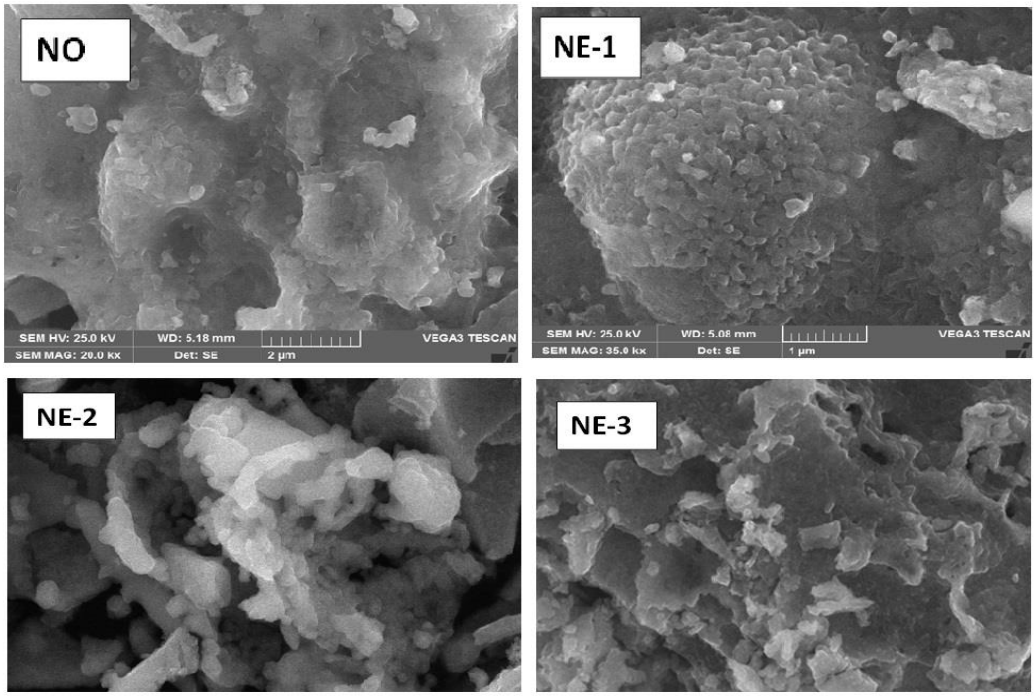

Figure 2. FE-SEM Micrographs of $Ni_{0.5}Sr_{0.5}Er_xFe_{2-x}O_4$ (NO($x=0.00$), NE-1($x=0.01$), NE-2($x=0.05$) and NE-3($x=0.09$) nanoferrites

In the result of this aggregation, the particle size reduction was observed which is in agreement with the crystallite size obtained from XRD results. The line intercept procedure is helpful in estimating an average grain size using the relation: Gav = 1.5 L/ MN where M – magnification, L-total length of test line in m, N - total number of grains intercept. Based on the formula, the calculated particles sizes are in the range of 27-30 nm. The particle sizes are in the nanoscale range (1−100nm) so, FE-SEM analysis confirmed the formation of nanoparticles [32].

3.4. EDAX analysis

The percentage of each element in the synthesised NPs are recorded using energy dispersive X-ray analysis spectra shown in Figure S2 kept in a supplementary file. The spectra show the

presence of elements, Ni, Sr, Er, Fe and O in expected values. The spectra present no impurity, indicating the high purity of all the samples and confirming the high crystallinity of all the samples.

Table 3. Atomic % and weight % of $Ni_{0.5}Sr_{0.5}Er_xFe_{2-x}O_4$ (x=0.00<x<0.09) nanoferrites

$Ni_{0.5}Sr_{0.5}Er_xFe_{2-x}O_4$	X=0.00				X=0.01					X= 0.05					X= 0.09				
Elements	O	Sr	Fe	Ni	O	Sr	Fe	Ni	Er	O	Sr	Fe	Ni	Er	O	Sr	Fe	Ni	Er
Atomic %	21.75	22.97	44.58	10.70	27.05	6.34	49.43	13.17	4.02	67.07	15.13	17.75	6.30	1.05	52.04	7.27	31.53	2.34	6.72
Weight %	52.24	10.07	30.68	7.00	58.37	2.50	30.56	7.74	0.83	26.69	35.62	26.64	4.74	6.30	20.70	15.84	43.92	9.80	9.74

3.5. TGA analysis

The TGA experiment was performed using 10 mg of synthesised sample at a heating rate of 5 ℃/min in static air is showed in Figure 3. In the DSC-TGA curve, the results indicate three stages of weight loss at different temperature. In the first step, the weight loss at 71.68 ℃ is due loss of lattice water molecules. The second step of weight loss has occurred at 223 ℃ corresponding to exothermic at 250.56 ℃ Finally, the third peak at 592.49 ℃, indicate the establishment of ferrite nanoparticles [33].

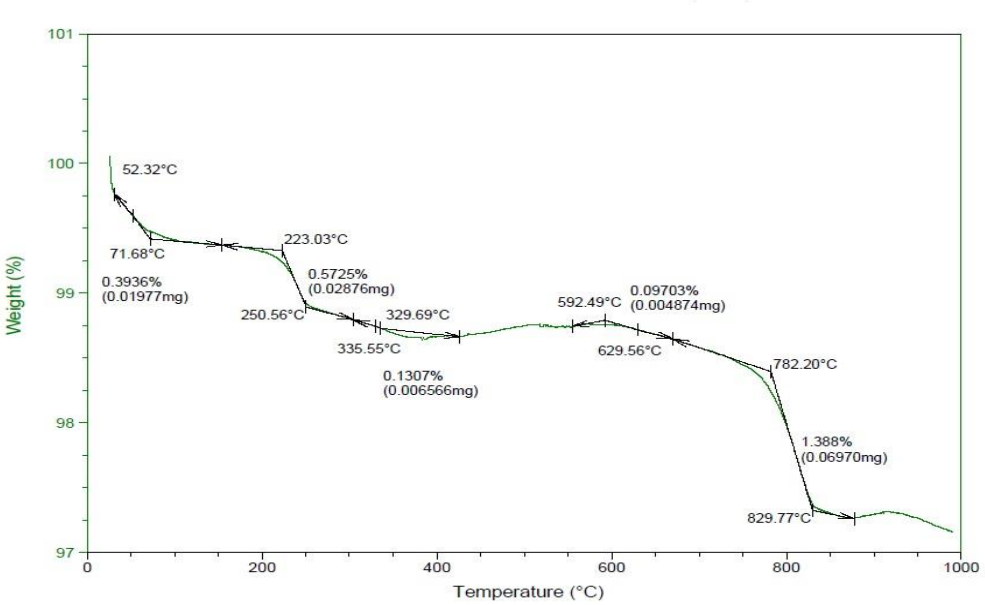

Figure 3. DSC-TGA curve of $Ni_{0.5}Sr_{0.5}Er_{0.09}Fe_{1.91}O_4$ nanoparticle

3.6. Optical properties

The UV–Visible spectra were determined for all the synthesised $Ni_{0.5}Sr_{0.5}Er_xFe_{2-x}O_4$ (x =0.00 < x < 0.09) nanoferrites using Shimadzu-UV-2600 spectrophotometer. Absorption is measured in the range of 200 - 800 nm. Using the equation Kubelka-Munk (K-M) model to get optical reflection spectra and F(R) was calculated from the following conditions. All Er^{3+} doped nanoparticles were analysed to obtain optical band gap.

$$Eg = \frac{hc}{\pi\lambda} = \frac{1240}{\lambda} \qquad (9)$$

$$F(R\infty) = \frac{(1-R\infty)^2}{2R\infty} \qquad (10)$$

$$\{(F(R\infty)\, h\nu\}^{1/n}(h\nu\text{-}Eg) \qquad (11)$$

Where: h is the Planck constant (6.626 x 10^{-34} Js), C-Speed of light (2.99×10^8 ms^{-1}), λ-Wavelength of reflectance spectra, R_∞- Diffuse reflectance spectra,α -Absorption coefficient, ν -Frequency of the incident light, Eg -Bandgap energy, n = 2 for direct bandgap.

The absorption spectrum of pure $Ni_{0.5}Sr_{0.5}Er_xFe_{2-x}O_4$ (x=0.00<x<0.09) showed in supplementary file Figure S3 indicate two characteristic absorption peaks attributed to the conducting emeraldine salt, one is around 285 nm and the other is at 430 nm. The first absorption band assigned at ~300 nm is due to the π-π* electronic transitions and the other is assigned at 435 nm due to the polaron band also representing the presence of lone pair electrons of nitrogen [33-35]. The absorption increases with increasing Er^{3+} concentration of $Ni_{0.5}Sr_{0.5}Fe_{2-x}O_4$ nanocomposites. In accordance with Beer's law, the absorption is proportional to the number of absorbing molecules. These results suggest that there are interactions with $Ni_{0.5}Sr_{0.5}Er_xFe_{2-x}O_4$ nanoparticles.

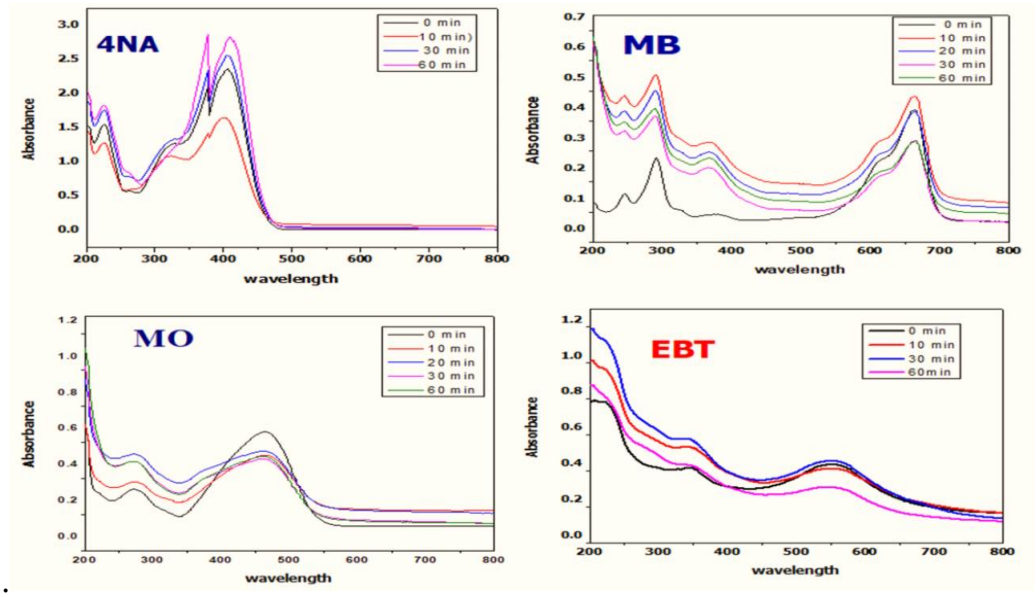

Figure 4. Band gap energy of $Ni_{0.5}Sr_{0.5}Er_xFe_{2-x}O_4$ (x=0.00<x<0.09) nanoferrites

The direct energy band gap (E_g) values were obtained by extrapolating the linear part of the $(\alpha h\upsilon)2$ curve versus $(h\upsilon)$ as shown in Figure 4. The energy band gap (E_g) values are tabulated in Table 3. It is clear that the band gap 2.5 eV of the Er^{3+} doped nickel nanoferrites samples when compared to pure $NiFe_2O_4$. The shift in band gap of the $Ni_{0.5}Sr_{0.5}Er_xFe_{2-x}O_4$ nanoparticles with decreasing crystallite size is the result of quantum confinement effects arising from the small size regime [35].

Table 4. UV-Vis absorption band gap values of $Ni_{0.5}Sr_{0.5}Er_xFe_{2-x}O_4$ ($x=0.00<x<0.09$)

Samples abbreviation	Time	Samples	Wavelength	Absorbance	% Degradation of dye
NO	0	$Ni_{0.5}Sr_{0.5}Fe_2O_4$	405.00	2.82	0
NE-1	10	$Ni_{0.5}Sr_{0.5}Er_{0.01}Fe_{1.99}O_4$	405.08	2.56	10.6
NE-2	30	$Ni_{0.5}Sr_{0.5}Er_{0.05}Fe_{1.95}O_{19}$	406.18	2.31	16.63
NE-3	60	$Ni_{0.5}Sr_{0.5}Er_{0.09}Fe_{1.91}O_{19}$	409.35	1.66	41.94

3.6. VSM Analysis

The magnetic properties of the samples were determined by vibrating sample magnetometer (VSM) (Make: CREST, Model: 20130523-01). The magnetic hysteresis loops of $Ni_{0.5}Sr_{0.5}Er_xFe_{2-x}O_4$ measured at room temperature are shown in Figure 5. It can be observed from M–H loops that soft magnetic behaviour exists for the pure and erbium doped nickel ferrites with a decrease in magnetization and increase in the concentration of Er^{3+} ions ($x=0.00<x<0.09$).

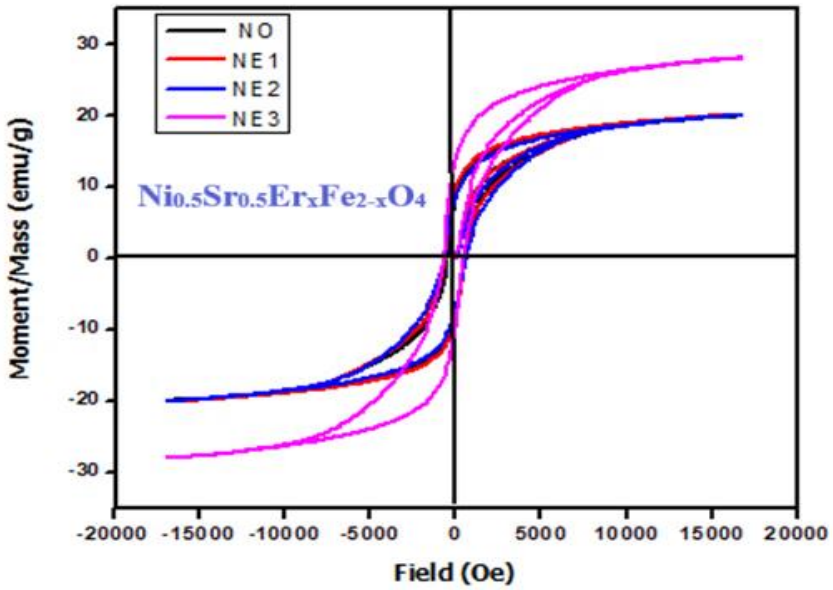

Figure 5. Hysteresis curves of $Ni_{0.5}Sr_{0.5}Er_xFe_{2-x}O_4$ ($x=0.00<x<0.09$) nanoferrites

MH curves provide the information about saturation magnetization (Ms), remanence Coercivity (Hc), magnetization (Mr), Magneton number (ηB), squareness ratio (S), anisotropy constant (K) and Yafet-Kittle angle α(Y-K) fields. The magnetic parameters are calculated using the following relations [36,37] of the sample and Table 4.

$$S = \frac{Mr}{Ms} \qquad (12)$$

Where Mr is remanent magnetization, Ms is saturation magnetization (emu/g), Hc is the coercivity and k = 0.64 is constant magnetic anisotropy. Yafet and Kittel angles are given by the equation and the Magneton number (ηB) values were obtained from the following equation.

$$\eta B = \frac{M\ X\ Ms}{5585} \qquad (13)$$

Where MW is the molecular weight of the composition (x) in g, ηB is the magnetic moment (number of Bohr magnetrons), Ms is saturation magnetization (emu/g), 5585 is the magnetic factor. The magnetic properties of the $NiFe_2O_4$ with an inverse spinel structure can be explained in terms of the cations distribution and magnetization originates from Sr^{2+} and Fe^{3+} ions have A-A exchange at tetrahedral sites, due to B-B interactions Ni^{2+}, Fe^{3+}, and Er^{3+} ions have at octahedral sites. A-B super exchange interaction in both the tetrahedral and octahedral ions was observed [38,39]. Hysteresis loops in Figure 5 are typical for soft magnetic materials and the 'S' shape of the curves together with the negligible coercivity (Hc = ≤ 0.60 Qe) shows the presence of magnetic particles exhibiting super paramagnetic behaviors [40-42].

The observed magnetic behaviour of the present samples can also be explained on the basis of Neel's model [43]. According to Neel, the Neel's magnetic moment (calculated magneton number) is given by MS = MB - MA, where MA is magnetic moment of A sublattice and MB is the magnetic moment of B sublattice. It is known that the spinel crystal structure consists of two interstitial sites namely tetrahedral (A) and octahedral [B] sites. Among these interstitial sites, the inter sublattice A-B superexchange interaction and intra sublattice A-A and B-B superexchange interaction exits. A-B interaction is much stronger than the A-A interaction and B-B interaction. The values of MB and MA are calculated considering the following cation distribution based on the site preference energy of the Er^{3+} (7 μB) replaces Fe^{3+} (5 μB) in an octahedral position (B site), and Er^{3+} has higher spin magnetic moment ions than Fe^{3+}. The substitution of Er^{3+} ions at the B site will affect the interaction between Ni–O–Er ions, and affect the sublattice exchange energy between Ni–O– Fe [44].

The magnetic moment of the Fe^{2+} ion decreased with the increase of the Er^{3+} ions, this action for this increase in value is due to the increasing of the super exchange interaction between the different sites, leading to an increase in the values (1.14-1.69 μβ). This shows that super-exchange interactions increase. Magnetization values of the $Ni_{0.5}Sr_{0.5}Er_xFe_{2-x}O_4$ samples are increased from for Ms 19.92 emu/g – 28.02 emu/g with an increase of the Er^{3+} ion content. Mr in the range of 8.20-12.13 emu/g at room temperature. Hc is in the scope of 466-606 Oe at room temperature. This reduction is associated with the equivalent reduction of Fe^{3+} ions to

charge-compensating Fe^{2+} ions replacing Er^{3+} ions. Moreover, the magnetic moment of Fe^{2+} ions (4 μB) is lower than that of the Fe^{3+} ions (5 μB) [45-47].

Table 5. Saturation magnetization (Ms), retentivity (Mr), coercivity (Hc) and magnetic moment (μB) of type hexaferrites for all compositions of $Ni_{0.5}Sr_{0.5}Er_xFe_{2-x}O_4$ (x=0.00<x<0.09)

Sample name	Ms(emu/g)	Mr(emu/g)	Mr/Ms	Hc(Oe)	nβ(uβ)
NO	19.924	8.2084	0.41198	466.60	1.148
NE-1	20.056	8.5927	0.42843	538.11	1.154
NE-2	19.973	7.4885	0.37493	604.111	1.811
NE-3	28.029	12.136	0.43298	606.74	1.691

Table 5 indicate variation of Ms and Mr. Variations in disorder and electronic states in cubic system causes ionic radii strains [48]. The squareness ratio values are observed in the scope of 0.37–0.43 emu/g show that the particles are in the single magnetic domain and those < 0.5 represent the particles with a multi-domain structure [49,50].

3.8. Electrochemical studies

3.8.1 Electrochemical study of different electrode

The cyclic voltammogram was performed to investigate the electrochemical properties of the synthesized $Ni_{0.5}Sr_{0.5}Er_xFe_{2-x}O_4$ molecule. The 0.1 mM $Ni_{0.5}Sr_{0.5}Er_xFe_{2-x}O_4$ in DMF were carried out with the pristine GCE as the working electrode scan at 20 mVs^{-1} in an inert nitrogen. Further $Ni_{0.5}Sr_{0.5}Er_xFe_{2-x}O_4$ /GCE electrode was dried and washed with deionised water and rinsed in DMF and employed for electrocatalytic sensor studies. The bare electrode showed redox peaks with very small peak currents, the $Ni_{0.5}Sr_{0.5}Er_xFe_{2-x}O_4$/GCE peaks are in agreement with the solution CV peaks enhanced, the peaks indicating the successful modification of the electrode surface with $Ni_{0.5}Sr_{0.5}Er_xFe_{2-x}O_4$. The voltammogram of the $Ni_{0.5}Sr_{0.5}Er_xFe_{2-x}O_4$ /GCE demonstrate redox peaks signifying that the designed compound is redox active. The redox peak raised between 0.3567–0.3644 V can be ascribed in Figure 6 [51,52].

Figure S6 exhibits the electrocatalytic redox peak of mercury from developed $Ni_{0.5}Sr_{0.5}Er_xFe_{2-x}O_4$ /GCE using synthesised nanoparticles in PBS pH 7 at a scan rate 20 mVs^{-1}. The catalytic peak observed at 0.36 V is due to the electro-catalytic redox reaction which was noticed from the mercury analyte at the $Ni_{0.5}Sr_{0.5}Er_xFe_{2-x}O_4$/GCE. The peak current at bare GCE was very minimal and the redox peak appeared at a higher positive overpotential. The bare/GCE in contrast to that of $Ni_{0.5}Sr_{0.5}Er_xFe_{2-x}O_4$, is represented. The $Ni_{0.5}Sr_{0.5}Er_xFe_{2-x}O_4$ /GCE showed enhanced peak current due to the fact that the resistive in nature for the charge transfer at the electrode as well as an increased corresponding concentration of mercury in an

electrolyte. It may be accountable for the efficient electrocatalytic redox peak current of mercury. The long linearity curve in the 80-180 µM/L with LOD value of 4.8008 µM/L and sensitivity of 6.219 $\mu A \mu M^{-1} cm^{-2}$. The value reveals an outstanding behaviour parameter of the developed $Ni_{0.5}Sr_{0.5}Er_xFe_{2-x}O_4$ /GCE sensor and acts as a good bioactive sensor compared with the previously detecting mercury presented in Table 5 [53].

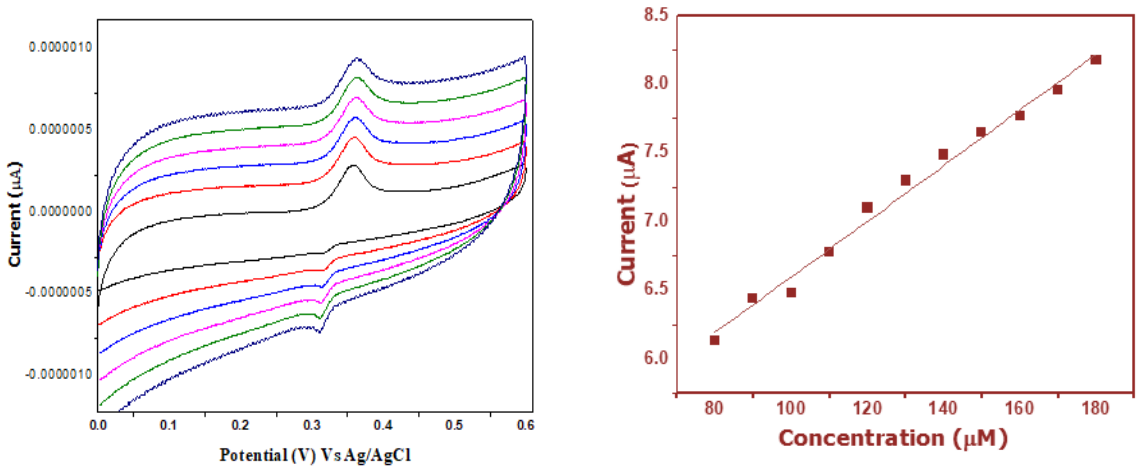

Figure 6. Cyclic voltammograms of $Ni_{0.5}Sr_{0.5}Er_xFe_{2-x}O_4$ /GCE at a) Different concentrations of Hg^{2+} 0.5-80 µM/L b) Calibration graph of peak current vs concentration of Hg^{2+} at scan rate 50 mVs^{-1}

3.8.2. Charge transfer behaviour of modified electrode

The charge transfer behaviour of $Ni_{0.5}Sr_{0.5}Er_xFe_{2-x}O_4$ modified sensor was investigated using $K_4[Fe(CN)_6]$, which behaves as a redox system. The bare glassy carbon electrode (GCE) displayed the Ferri/ferrocyanide system in CV response. The electrochemical evaluation in 0.5 mM $K_4[Fe(CN)_6]$ solution at a scan rate of 50 mVs^{-1} between bare GCE and modified $Ni_{0.5}Sr_{0.5}Er_xFe_{2-x}O_4$ /GC electrodes is represented in supplementary file Figure S6. Bare GCE shows a current response is 4.344×10^{-5} A and modified GCE exhibited a more current response such as 5.646×10^{-5}A in the redox system because the modified GCE has good electro-conducting properties compared to bare GCE. The electrode acts as a bridge of electron transfer between the electrode surface (GCE) and buffer solution in a cyclic voltmeter [54].

3.8.3. Electrochemical investigation of the different electrodes

Electrochemical sensing of mercury was studied in an electrolytic solution using a phosphate buffer solution of pH 7. The cyclic voltammogram of (i) bare GCE, (ii) $Ni_{0.5}Sr_{0.5}Er_xFe_{2-x}O_4$ /GCE, with 100 µL concentration of mercury at a scan rate of 20 $mVs^{-1.}$ The modified $Ni_{0.5}Sr_{0.5}Er_xFe_{2-x}O_4$/GCE electrode showed intensified peak current responses as compared to the bare glassy carbon electrode, and it is a good electrochemically active, as represented in Figure 7 [55].

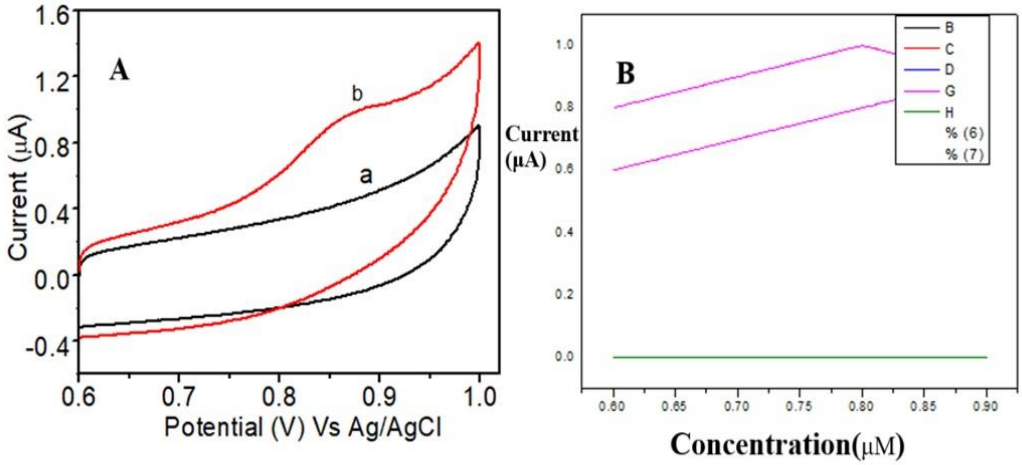

Figure 7. Cyclic Voltammograms of A) Electrochemical investigation of the different electrodes (a) GCE (bare electrode) (b) $Ni_{0.5}Sr_{0.5}Er_xFe_{2-x}O_4$ /GCE B) Linear relationship between current and concentration of Hg^{2+} at scan rate 50 mVs^{-1}

3.8.4. Effect of scan rate

The scan rate was investigated and the effect of different scan rates 10 to 60 mVs^{-1} on an immobilized sensor $Ni_{0.5}Sr_{0.5}Er_xFe_{2-x}O_4$/GCE indicated that it was determined a linear relationship between peak current and scan rate as presented in Figure 7B.

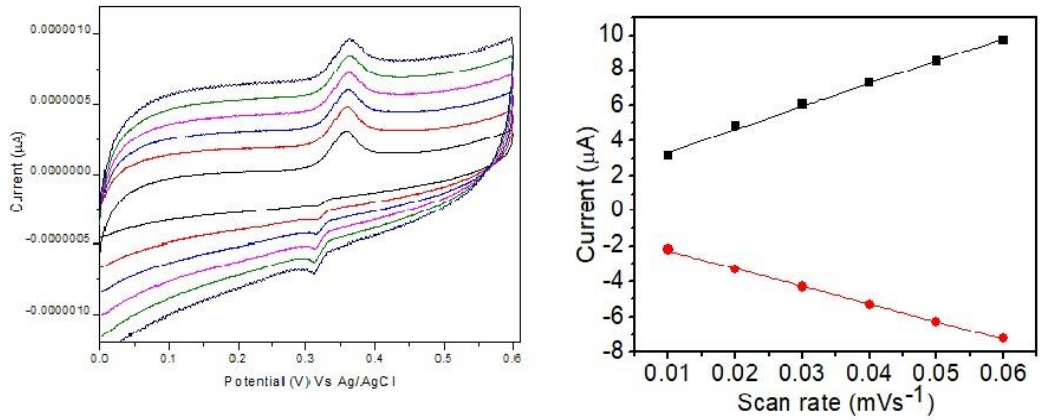

Figure 8. (a) Cyclic voltammogram of Hg^{2+} at $Ni_{0.5}Sr_{0.5}Er_xFe_{2-x}O_4$ modified GCE scan rate ranging from (10-150 mVs^{-1}) (b) Inset calibration graph of the square root of scan rate vs peak current

In addition to this, a plot of peak current vs scan rate highlighted in Figure 8 emphasizes that it is a diffusion-controlled process with a correlation coefficient of 0.8954 $\mu A \mu M^{-1} cm^{-2}$, sensitivity 7.135 $\mu A \mu M^{-1} cm^{-2}$ and linear regression equation denoted as I_{pa}=8.994 + 0.480, it is further observed that electrochemical process of mercury is a surface adsorbed process [56].

3.8.4. Differential pulse voltammetry (DPV) studies of mercury

DPV was one of the best techniques for detecting mercury using modified $Ni_{0.5}Sr_{0.5}Er_xFe_{2-x}O_4$ /GCE, and it gives accurate results for the detection of Mercury, it was conducted in PBS pH 7, and the results are collected in Table 4. The reaction which occurs, as mentioned below, showed enhanced anodic peak current response compared to bare GCE. The increasing concentration of mercury in the range from 20 to 100 $\mu molL^{-1}$ and the peak current enhanced at the fixed potential. The analytical profile of the modified electrode was a long linear range 20 to 100 $\mu mol\ L^{-1}$, sensitivity 0.0113 $\mu A\mu M^{-1}cm^{-2}$ and LOD is 6.667 $\mu molL^{-1}$. Further, the modified sensor shows reproducible and anti-leaching properties [57-67], as shown in Figure 9.

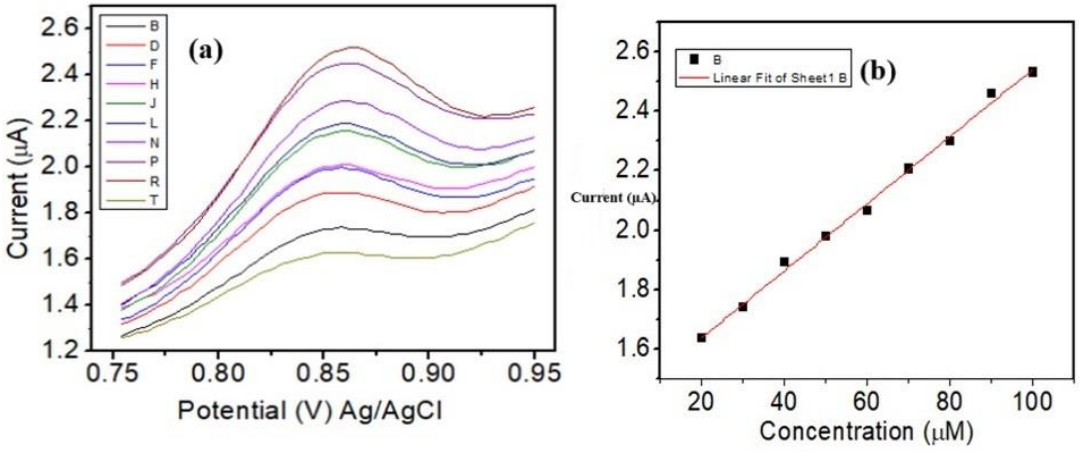

Figure 9. (a) DPV of $Ni_{0.5}Sr_{0.5}Er_xFe_{2-x}O_4$ /GCE at a concentration ranging from 20–100 µM (b) Linear graph of current (µA) *vs.* Concentration (µM)

Table 6. Comparison of the different actuators for mercury determination

Compound	Linear range $\mu molL^{-1}$	Technique	LOD µmol L^{-1}	Sensitivity ($\mu A\ \mu M^{-1}\ cm^{-2}$)	Ref.
CoTM-QOPc /CNP/GCE	0.2-200	CV	0.06	2.298	[15]
	0.2-225	DPV	0.06	1.031	
CoL/MNSs/CPE	0.2-30.0	SWV	0.015	-	[39]
Co_3O_4/RGO	1-380	CV	0.14	29.5	[40]
CRS/BN RGO/GCE	0.001- 1290	DPV	0.0159	1.5309	[41]
$Ni_{0.5}Sr_{0.5}Er_xFe_{2-x}O_4$	50-190	CV	16.66	0.00647	**Present work**
	20-100	DPV	6.667	0.0113	

The comparison of the efficiency of the present electrode with the different modified electrodes reported in the literature in terms of their sensitivity, limit of detection (LOD) and

linearity used CV method was done in Table 6. The cyclic voltammetry analysis demonstrates that the electrode used in the present study has a higher sensitivity for detecting Hg^{+2} than those reported in previously reported ones. Additionally, although the limit of detection is slightly higher, the linear range of detection is wider, indicating a better performance in detecting varying concentrations of Hg^{+2}.

4. CONCLUSION

A series of rare earth Er^{3+} doped $Ni_{0.5}Sr_{0.5}Fe_2O_4$ nanoparticles were prepared by the self-propagation method. The room temperature XRD patterns verified the existence of cubic spinel structure. Crystallite size of the synthesized sample is 27-30 nm. Two metal-oxygen (M–O) vibration modes were revealed by FT-IR spectra within the range of 1500 to 350 cm^{-1} confirming the successful formation of spinel ferrites and the force constant the KT values were less than the KO values in the samples substituted with Er^{3+} ions. FE-SEM micrograph images confirmed that the morphological structure is aggregated to the size of nanoparticles. The EDX spectrum confirms the doping concentration and freedom from impurity elements. The Tauc plots revealed an indirect allowed band gap in the range of 2.5 eV. The VSM analysis of coercivity showed a peak with particle size at a value smaller than the previously reported value of single-domain limit for $Ni_{0.5}Sr_{0.5}Er_xFe_{2-x}O_4$ that has been attributed to the enhanced role of the surface anisotropy as compared to the bulk for small sizes, which is the result of the reduction in superexchange interaction. The electrochemical study by modified electrode $Ni_{0.5}Sr_{0.5}Er_xFe_{2-x}O_4$/GCE showed well-established redox behaviour and exhibited good results in the investigation of mercury by CV. In addition, the biocompatibility and synergistic effect of $Ni_{0.5}Sr_{0.5}Er_xFe_{2-x}O_4$/GCE indicate an enhanced sensitivity is 4.059 ($\mu A\ \mu M^{-1}\ cm^{-2}$), LOD is 3.333 µmol/L and the modified electrode exhibited good sensitivity, selectivity and stability. The spectrochemical, pharmaceutically, and electrochemical results suggest that the synthesised compounds act as drugs. It has been found that the spinel $Ni_{0.5}Sr_{0.5}Er_xFe_{2-x}O_4$ nanopowders doped with x = 0.5 of Er^{3+} ions exhibit higher antibacterial efficiency against *Staphylococcus aureus* and *Klebsiella pneumonia* compared with other compositions, due to their smaller particle size and higher surface area, which enhanced the better active sites.

Acknowledgement

We extended our thanks USIC, University of Guwahati, Assam for providing the VSM spectral data, SAIF, Karnataka University, Dharwad for providing TGA spectral data. and VGST-K-FIST(L1), Karnataka Government, Karnataka, India.

Declarations of interest

The authors declare no conflict of interest in this reported work.

REFERENCES

[1] T. Diing, E.A. Level, and O. Cadar, Nanomaterials 11 (2021) 1560.
[2] V.L. Mathe, and R.B. Kamble, Mater. Res. Bull. 48 (2013) 1415.
[3] M. Salavati-Niasari, F. Davar, and T. Mahmoudi, Polyhedron 28 (2009) 1455.
[4] A. Alarifi, N.M. Deraz, and S. Shaban, J. Alloys Compounds 486 (2009) 501.
[5] Y. Kinemuchi, K. Ishizaka, H. Suematsu, W. Jiang, and K. Yatsui, Thin Solid Films 407 (2002) 109.
[6] P.B. Kharat, A.V. Humbe, and J.S. Kounsalye, J. Supercond. Magn 32 (2020) 1644.
[7] P.B. Kharat, B.S. Somvanshi, P.P. Khirade, and K.M. Jadhav, ACS Omega 36 (2020) 23378.
[8] B. Sandeep. Somvanshi, P.B. Kharat, M.V. Khedkar, and K.M. Jadhav, J. Physics Conference Series 1644 (2020) 12028.
[9] R.M. Borade, B. Sandeep. Somvanshi, B. Swati, P. Rajendra, and K.M. Jadhav, Mater Res. Express (2020) 7.
[10] K.S. Jithendra Kumara, G. Krishnamurthy, N.S. Kumar, N. Naik, T.M. Praveen, J. Magn Magn Mater 451 (2021) 457.
[11] K.S.J. Kumara, G. Krishnamurthy, B.E. Kumara Swamy, N.D. Shashi Kumar, S. Naik, B.S. Krishna, and N. Naik, A Organ Chem. 31 (2016).
[12] M. Veena, A. Somashekaraa, G.J. Shankaramurthy, H.S. Jayanna, and H.M. Somashekaraa, J. Magn. Magn. Mater. 419 (2016) 375.
[13] M.N. Ashiqa, M.F. Ehsana, M.J. Iqbalb, and F.H. Gulc, J. Alloys Compd. 509 (2011) 5119.
[14] F. Cheng, C. Liao, J. Kuang, Z. Xu, C. Yan, L. Chen, H. Zhao, and Z. Liu, J. appl. Phys. 85 (1999) 2782.
[15] G. Dascalu, G. Pompilian, B. Chazallon, V. Nica, O.F. Caltun, S. Gurlui, and C. Focsa, Ceramics Int. 40 (2014) 14533.
[16] X. Chena, J. Zhaoa, J. Wanga, Y. Liua, L. Wanga, R. Weerasooriyaa, Y. Wua, Electrochim. Acta 387 (2021) 138539.
[17] N.K. Vasantakumarnaik, G. Krishnamurthy, M. Pari, J. Survey in Fisheries Sci. 10 (2023) 4.
[18] R.S. Yadav, I. Kuřitka, J. Vilcakova, J. Havlica, L. Kalina, P. Urbánek, M. Machovsky, D. Skoda, M. Masař, and M. Holek, Ultrasonics Sonochem. 40 (2018) 773.
[19] P. Sivakumar, R. Ramesh, A. Ramanand, S. Ponnusamy, and C. Muthamizhchelvan, J. Alloys and Compounds 537 (2012) 203.
[20] M.N. Akhtar, and M.A. Khan, J. Magn. Magn. Mater. 32 (2021) 7692.
[21] D. Makovec, A. Košak, A. Žnidaršič, and M. Drofenik, J. Magn. Magn. Mater. 289 (2005) 32.

[22] K. Maaz, S. Karim, A. Mumtaz, S.K. Hasanain, J. Liu, J. L. Duan, J. Magn. Magn. Mater. 27 (2016) 2601.
[23] J. Lakshmikantha, G. Krishnamurthy, B.M. Nagabhushan, C.S. Naveen, and E. Melagiriyaa, J. Supercond Nov. Magn. 35 (2022) 2485.
[24] T. Prabhakaran, and J. Hemalatha, J. Alloys Compd. 509 (2011) 7071.
[25] L. Guo, X. Shen, and Y. Feng, J. Alloys Compd. 490 (2010) 301.
[26] A.K. Nikumbh, A.V. Nagawade, G.S. Gugale, M.G. Chaskar, and P.P. Bakare, J. Mater. Sci. 37 (2002) 637.
[27] D.R. Lide, CRC Handbook of Chemistry and Physics, 76th ed, CRC Press, London (1995).
[28] M. Srivastava, S. Chaubey, and A.K. Ojha, Mater. Chem. Phys. 118 (2009) 174.
[29] K.B. Modi, S.J. Shah, N.B. Pujara, T.K. Pathak, N.H. Vasoya, and I.G. Jhala, J. Mol. Struct. 1049 (2013) 250.
[30] M. Rahimi, P. Kameli, M. Rajbar, H. Hajihashemi, and H. Salamati, J. Mater. Sci. 48 (2013) 2969.
[31] K. Nakamoto, D. Huang, and R. Wang, Beijing (1986) 231.
[32] Z. Noreen, I. Ahmad, F. Siddiqui, A.B. Ziya, T. Abbas, and H. Bokhari, Ceram Int. 43 (2017) 10784.
[33] B.S. Holinsworth, D. Mazumder, H. Sims, Q.C. Sun, M.K. Yurtisigi, S.K. Sarker, A. Gupta, W.H. Buther, and J.L. Musfeldt, Phys. Lett. 103 (2013) 082406.
[34] Q.C. Sun, H. Sims, D. Mazumder, J.X. Ma, B.S. Holinsworth, K.R.O. Neal, G. Kim G, W.H. Butler, A. Gupta, and J.L. Musfeldt, Rev. B. 86 (2012) 205106.
[35] T. Vigneswari, and P. Raji, Int. J. Mater. Res. 109 (2018) 413.
[36] J. Lakshmikantha, G. Krishnamurthy, B.M. Nagabhushan, and E. Melagiriyaa, J. Solid State Chem. 315 (2022) 123465.
[37] J. Lakshmikantha, G. Krishnamurthy, R.H. Nayak, M. Pari, N. Ranjitha, and N. Naik, Inorganic Chem. Commun. 146 (2022) 110175.
[38] M. Chand, A. Kumar, K.S. Annveer, and A. Shankar, Ind. J. Eng. Mater. Sci. 18 (2011) 385.
[39] K. Zipare, J. Dhumal, S. Bandgar, V. Mathe, G. Shahane, J Nanosci. Nanoeng. (2015) 178.
[40] E. Manova, T. Tsoncheva, C. Estournes, D. Paneva, K. Tenchev, I. Mitov, Al. Catal. A 6 (2006) 170.
[41] R.H. Kodama, A.E. Berkowitz, and E.J McNi. Phys. Rev. Lett. 77 (1996) 394.
[42] A.A. Kadam, S.S. Shinde, S.P. Yadav, P.S. Patil, and K.Y. Rajpure, J. Magn. Magn. Mater. 329 (2013) 59.
[43] S. Alone, S.E. Shirsath, R. Kadam, and K. Jadhav, J. Alloys Compd, 509 (2011) 5055.

[44] L.B. Tahar, M. Artus, S. Ammar, L. Smiri, F. Herbst, M.J. Vaulay, V. Richard, J.M. Grenèche, F. Villain, F. Fievet, J. Magn. Magn. Mater, 320 (2008) 3242.

[45] A. Nikumbh, R. Pawar, D. Nighot, G. Gugale, M. Sangale, M. Khanvilkar, A. Nagawade, J. Magn. Magn. Mater. 355 (2014) 201.

[46] O.M. Hemeda, M.Z. Said, and M.M. Barakat, J. Magn. Magn. Mater. 224 (2001) 132.

[47] A.B. Nawale, N.S. Kanhe, K.R. Patil, S.V. Bhoraskar, and V.L. Mathe, J. Alloys Compd. 509 (2011) 4404.

[48] H. Nathani, and R.D.K. Misra, Mater. Adv. Technol. 113 (2004) 228.

[49] J. Hu, Y. Ma, X. Kan, C. Liu, X. Zhang, R. Rao, M. Wang, and G. Zheng, J. Magn. Magn. Mater. (2020).

[50] K.B. Modi, M.K Rangolia, M.C. Chhantbar, and H.H. Joshi, J. Mater. Sci. 41 (2006).

[51] T.P. Poudel, B.K. Rai, S. Yoon, D. Guragain, D. Neupane, S.R. Mishra, T.P. Poudel, B.K. Rai, S. Yoon, D. Guragain, D. Neupane, and S.R. Mishra, J. Alloy. Compd. 802 (2019) 609.

[52] S. Yoon, and K.M Krishnan, J. Al. Phys. 109 (2011) 07B534.

[53] Y. Yaffet, and C. Kittel, Phys. Rev. 47 (2018) 3608.

[54] R.S. Turtelli, G. Jilani, B.S. Mounesh, P. Malathesh. C.D. Mruthyunjayachari and K.R.V. Reddy, J. Mater. Chem. Phys. (2020).

[55] M. Parsaei, Z. Asadi, and S. Khodadoust, Sens. Actuators B 220 (2015) 1131.

[56] Y. Haldorai, Y.J. Kim, V.E. Nam-Su, Y.H. Huh, and K. Hana, Sens. Actuators B 27 (2016) 27.

[57] V. Mariyaan, M.S. Chen, K. Murugan, A. Jeevika, T. Jeyapragasam, and R. Ramachandra, Physicochem. Engin. Aspects (2022) 637.

[58] Y.N. Wang, Y.Y. Wu, L. Yang, X.Q. Qi, Adv Mater. Res. (2013) 781.

[59] N. Vasantakumaranaik, G. Krishnanaik, P. Malathesh, N. Venugopal, and N. Nagarajanaik, Biointerface Res. Appl. Chem. (2023) 531.

[60] K. Chitra, K. Reena, A. Manikandan, and S.A. Antony, J. Nanosci. Nanotech. 15 (2015) 4984.

[61] N. Babitha, L. Srimathi Priya, S. Rosy Christy, A. Manikandan, A. Dinesh, M. Durka, and S. Arunadevi, J. Nanosci. Nanotech. 19 (2019) 2888.

[62] K. Chitra, A. Manikandan, S. Moortheswaran, K. Reena, and S. Arul Antony, Adv. Sci. Eng. Med. 7 (2015) 710.

[63] V. Sumithra, A. Manikandan, M. Durka, S. K. Jaganathan, A. Dinesh, N. Ramalakshmi, and S. Arul Antony, Adv. Sci. Eng. Med. 9 (2017) 483.

[64] K. Chitra, A. Manikandan, and S. Arul Antony, J. Nanosci. Nanotech. 16 (2016) 758.

[65] A. Manikandan, E. Manikandan, B. Meenatchi, S. Vadivel, and S.K. Jaganathan, J. Alloys Compds. 723 (2017) 1155.

[66] R. Bomila, S. Srinivasan, S. Gunasekaran, and A. Manikandan, J. Supercond. Nov. Magn. 31 (2018) 855.